La radiologia medica (2024) 129:737–750
https://doi.org/10.1007/s11547-024-01803-0

BREAST RADIOLOGY

Nomogram for preoperative differentiation of benign and malignant breast tumors using contrast-enhanced cone-beam breast CT (CE CB-BCT) quantitative imaging and assessment features

Tong Su[1] · Yineng Zheng[1] · Hongyu Yang[2] · Zubin Ouyang[1] · Jun Fan[1] · Lin Lin[1] · Fajin Lv[1]

Received: 8 September 2023 / Accepted: 14 February 2024 / Published online: 21 March 2024

Abstract

Purpose Breast cancer's impact necessitates refined diagnostic approaches. This study develops a nomogram using radiology quantitative features from contrast-enhanced cone-beam breast CT for accurate preoperative classification of benign and malignant breast tumors.

Material and methods A retrospective study enrolled 234 females with breast tumors, split into training and test sets. Contrast-enhanced cone-beam breast CT-images were acquired using Koning Breast CT-1000. Quantitative assessment features were extracted via 3D-slicer software, identifying independent predictors. The nomogram was constructed to preoperative differentiation benign and malignant breast tumors. Calibration curve was used to assess whether the model showed favorable correspondence with pathological confirmation. Decision curve analysis confirmed the model's superiority.

Results The study enrolled 234 female patients with a mean age of 50.2 years (SD ± 9.2). The training set had 164 patients (89 benign, 75 malignant), and the test set had 70 patients (29 benign, 41 malignant). The nomogram achieved excellent predictive performance in distinguishing benign and malignant breast lesions with an AUC of 0.940 (95% CI 0.900–0.940) in the training set and 0.970 (95% CI 0.940–0.970) in the test set.

Conclusion This study illustrates the effectiveness of quantitative radiology features derived from contrast-enhanced cone-beam breast CT in distinguishing between benign and malignant breast tumors. Incorporating these features into a nomogram-based diagnostic model allows for breast tumor diagnoses that are objective and possess good accuracy. The application of these insights could substantially increase reliability and efficacy in the management of breast tumors, offering enhanced diagnostic capability.

Keywords Cone-beam computed tomography · Breast neoplasms · Logistic models · Nomograms · Diagnosis

Abbreviations

AUC	Area under the receiver operating curve
BI-RADS	Breast imaging reporting and data system
CB-BCT	Cone-beam breast CT
CE CB-BCT	Contrast-enhanced cone-beam breast CT
CI	Confidence interval
DCA	Decision curve analysis
DCIS	Ductal carcinoma in situ
ICC	Intraclass correlation coefficient
IQR	Interquartile range

Tong Su and Yineng Zheng have contributed equally to this work.

✉ Fajin Lv
fajinlv@163.com

Tong Su
sutong130910@163.com

Yineng Zheng
yinengzheng@cqmu.edu.cn

Hongyu Yang
2949084279@qq.com

Zubin Ouyang
ouyangzubin@aliyun.com

Jun Fan
382444209@qq.com

Lin Lin
278683576@qq.com

[1] Department of Radiology, The First Affiliated Hospital of Chongqing Medical University, No.1, Youyi Road, Yuanjiagang, Yuzhong District, Chongqing, China

[2] Department of Radiology, Chongqing Changshou District People's Hospital, Chongqing, China

MG	Mammography
MRI	Magnetic resonance imaging
NCE CB-BCT	Non-contrast-enhanced cone-beam breast CT
NME	Non-mass enhancement
OR	Odds ratio
ROC	Receiver operating characteristic
ROI	Region of interest
SD	Standard deviation
US	Ultrasound

Introduction

Breast tumors can be benign or malignant. Breast cancer, a highly malignant tumors originating in breast cells, is the leading cause of cancer-related deaths among females worldwide, with a rising global burden despite advancements in screening, diagnosis, and management [1]. Radiographic imaging is vital in breast cancer management, employing methods like breast ultrasound (US), mammography (MG), cone-beam breast CT (CB-BCT), and breast magnetic resonance imaging (MRI) to visualize breast tissue and detect potential malignant tumor indicators [2].

The Breast Imaging Reporting and Data System (BI-RADS), developed by the American College of Radiology, is a valuable tool for interpreting breast imaging findings, ranging from normal to highly suspicious of malignancy [3]. However, so far no standardized BI-RADS guidelines were published for CB-BCT and data on this field are limited. A more objective and accurate system is needed to evaluate breast tumors malignancy. The quantitative radiologic features offer a potential objective approach. Previous studies on quantitative radiologic features have predominantly concentrated on a single feature [4, 5]. However, the exclusive focus on a single feature may lead to the oversight of other crucial characteristics, resulting in limitations when assessing various aspects of the mass.

CB-BCT, utilizing a cone-beam X-ray generator and flat panel detector, combines the benefits of mammography and MRI, offering broad clinical potential. With the injection of contrast medium, contrast-enhanced cone-beam breast CT (CE CB-BCT) has demonstrated improved diagnostic efficiency compared to non-contrast-enhanced cone-beam breast CT (NCE CB-BCT) and mammography, and comparable sensitivity to MRI [6–9]. Considered the advantages of faster imaging speed, higher comfort level, fewer contraindications, and objective applications, CE CB-BCT holds promise as a valuable method in breast imaging [9–13].

In this study, we hypothesized that quantitative radiologic features of CE CB-BCT have the ability of predict benign and malignant breast tumors. We aim to develop and validate a nomogram based on quantitative radiologic features from CE CB-BCT to provide a more accurate and objective system for breast tumors diagnosis and management.

Methods

Study design

This retrospective study was approved by the institutional review board of our hospital (2022-K313). The requirement for the patients' informed consent was waived. A comprehensive workflow diagram of this study is presented in Fig. 1.

Patients

A total of 688 patients were initially reviewed for inclusion in this study, based on the following criteria: (a) patients who underwent CB-BCT scans between October 2019 and December 2022 and (b) breast tumors that were pathologically confirmed by operative specimens. The exclusion criteria were as follows: (a) patients who only underwent NCE CB-BCT scans ($n=216$); (b) patients who had previously undergone core biopsy or received treatment such as neoadjuvant therapy, lumpectomy, or radiation therapy before the CB-BCT scan ($n=76$); (c) non-mass enhancement (NME) lesions ($n=162$); since this study focused on evaluating the radiology quantitative features of breast tumors, a well-defined tumors boundary was needed. Consequently, 234 lesions from 234 female patients were included in the dataset. The included and excluded patients are summarized in a flow chart (Fig. 2). The dataset was split into training and test sets in a 7:3 ratio, with 70% used for training ($n=164$) to filter quantitative features and build the nomogram, and 30% ($n=70$) for testing to validate the nomogram's predictive performance [14–17]. This split ratio is chosen in logistic regression to balance accurate model parameter estimation and prevent overfitting or underfitting, ensuring the test set is adequately sized for reliable model evaluation [16].

Imaging acquisition

The CB-BCT images were acquired using the Koning Breast CT-1000 system by Corning Medical Equipment Co., Ltd. Patients were positioned prone on the scanning bed, allowing the breast to naturally hang into the scanning field. A 360° rotary scan of the breast was performed using the X-ray generator and flat plate detector. The imaging parameters included a fixed tube voltage of 49 kVp and variable tube currents (50–160 mA) adjusted for breast density and size. Following NCE CB-BCT scan, a nonionic iodine contrast agent (Ultravist®370, Bayer Healthcare Company Ltd.) was intravenously injected at a rate of 3.0 ml/s, with a dosage of 1.2–1.5 ml per kg of body weight, using a power injector

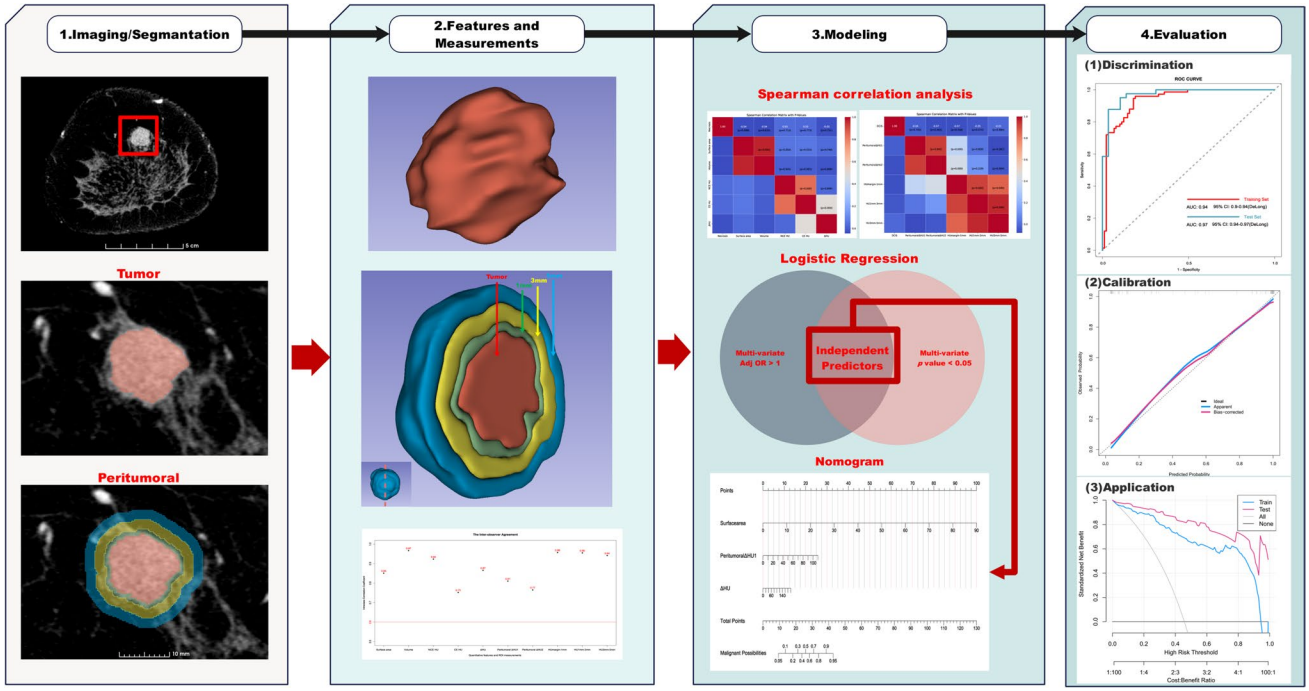

Fig. 1 Workflow diagram of the study. In the first column, the red solid box represents the tumors observed on contrast enhancement cone-beam breast CT (CE CB-BCT). The red mask indicates the region of interest (ROI) for the tumors. The peritumoral tissue surrounding the tumors is represented by multiple-color circles at different distances: tumors margin to peritumoral 1mm (green), peritumoral 1 mm to 3 mm (yellow), and peritumoral 3 mm to 5 mm (blue). In the second column, the top two plots display the ROI measurements and quantitative features obtained from 3-dimensional ROIs of the tumors and peritumoral tissue. The lowest plot shows scatter plot of intraclass correlation coefficient (ICC) for ROI measurements and quantitative features. In the third column, the compound heatmap at the top displays the Spearman correlation analysis results between features and measurements with necrosis or with peritumoral DCIS (Ductal carcinoma in situ). The binary Venn diagram illustrates the independent predictor variables of quantitative features in multiple-factor logistic regression. These variables satisfy the criteria of having an adjusted odds ratio (Adj OR) greater than 1 and a p-value less than 0.05. The independent predictors were used to construct the Nomogram model. In the last column, the plots depict the receiver operating characteristic (ROC) curves, calibration curves, and decision curve analysis (DCA). The plots are arranged from top to bottom in the given order

(MEDRAD®Stellant, Bayer Healthcare Company Ltd.). The side with the suspected mass was given priority, ensuring a 120 s delay before obtaining contrast-enhanced images. Prior to conducting the contrast-enhanced scan, comprehensive laboratory tests were performed to assess the patient's thyroid and renal function [18, 19]. To conduct a comprehensive CE CB-BCT scan, the procedure involves both a NCE CB-BCT scan preceding and a scan taken 120 s after the injection of contrast media. The calculated median Average Glandular Dose (AGD) for each breast in this procedure is 12.36 mGy, with an Interquartile Range (IQR) ranging from 11.25 to 13.35 mGy. Reconstruction was performed using the standard mode, resulting in isotropic three-dimensional images with a voxel size of 0.273 mm^3.

ROI segmentation

The segmentation of the region of interest (ROI) was conducted by four radiologists. To ensure an unbiased determination of the ROI, Radiologist 1 and Radiologist 2, unaware of the clinicopathological information of the patients, jointly delineated the entire tumor region layer by layer, resulting in a three-dimensional ROI for each lesion using 3D-slicer software (Version 5.2.1; www.slicer.org) [20]. During ROI segmentation, peri- and intra-tumoral calcifications were excluded to avoid biased. To enhance reproducibility in ROI determination, any inconsistencies between the two radiologists' segmentation were reviewed by a senior radiologist (Radiologist 3). Through discussion and consensus, any discrepancies were resolved to achieve a final ROI agreement.

Definition and measurement of quantitative features

We employed multiple quantitative features to measure breast tumors. All the quantitative features can be directly obtained or calculated based on the measurement results using the segment statistics module of 3D Slicer [20]. To gauge the reliability of each quantitative feature and ROI measurement, Radiologist 4 randomly selected 60 patients,

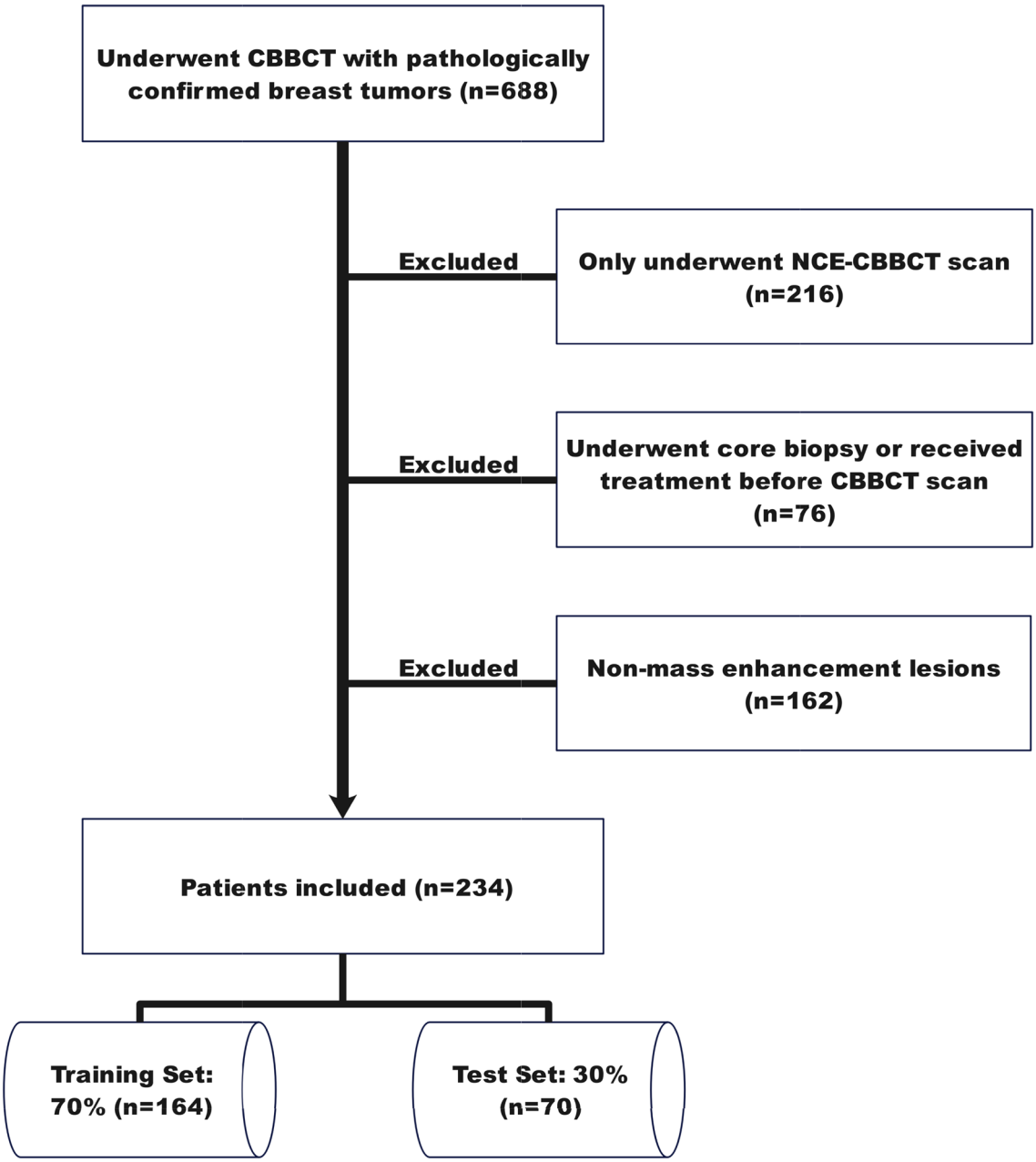

Fig. 2 Inclusion and exclusion of patients. Initially, 688 patients were considered, excluding: **a** those with only NCE CB-BCT scans ($n=216$); **b** individuals with prior core biopsy or treatment before CB-BCT ($n=76$); **c** cases with Non-mass enhancement (NME) lesions ($n=162$). This resulted in the inclusion of 234 lesions from 234 female patients. The dataset was then randomly divided into a 7:3 ratio, creating a training set ($n=164$) for filtering quantitative features and building the nomogram, and a test set ($n=70$) to validate the nomogram's predictive ability

independently performed ROI segmentation and feature measurement. The intraclass correlation coefficient (ICC) was computed for features and measurements [21]. To prevent bias from necrosis or peritumoral ductal carcinoma in situ (DCIS), in all the malignant patients, features and measurements showing significant associations in Spearman correlation analysis were excluded, particularly since these are commonly observed in malignant tumors.

These quantitative features can be categorized into three groups: the whole tumor's size, included volume and surface area; the whole tumor's CT value, included the CT values without contrast enhanced (NCE HU), the CT values after contrast enhanced (CE HU), and the degree of enhancement (ΔHU). In this study, we utilized the peritumoral delta HU (peritumoral ΔHU) as a unique characteristic to describe the peritumoral CT values after

enhancement. This value was computed based on the mean CT value of the tissues surrounding the tumors at specific distances. To mitigate the possibility that any findings would be a consequence of arbitrarily selected distance, we chose two different peritumoral ΔHU values. To obtain these values, we first defined the peritumoral areas based on the tumor's region of interest (ROI), and the peritumoral areas were radially expanded to the tumor's margin by 1 mm, 3 mm, and 5 mm, respectively. Next, using the segment statistics module of 3D Slicer, we measured the mean CT values of these peritumoral areas. The peritumoral ΔHU 1 and peritumoral ΔHU 2 were calculated by subtracting the mean CT value of the 1–3-mm regions ($HU_{1mm–3\ mm}$) and 3–5-mm regions ($HU_{3mm–5\ mm}$), respectively, from the mean CT value at 1 mm ($HU_{margin–1\ mm}$), using the following formulas (Fig. 3):

$$\text{Peritumoral } \Delta\text{HU } 1 = HU_{margin-1mm} - HU_{1mm-3mm}$$

$$\text{Peritumoral } \Delta\text{HU } 2 = HU_{margin-1mm} - HU_{3mm-5mm}$$

After that, we compared the performance of these two peritumoral ΔHU values in predicting benign and malignant tumors using receiver operating characteristic analysis (ROC) in the training set. The one with the greater area under the curve (AUC) was selected to join the quantitative features.

Development and validation of the nomogram model

We compared the differences in quantitative features between benign and malignant breast tumor in the training set. The logistic regression analysis was applied in the training set to identify independent predictors of quantitative features, which were then used to construct the nomogram for distinguishing between benign and malignant breast tumors. The nomogram can be characterized by summing up points assigned to each variable, as indicated at the top of the scale. To determine points for each predictor, draw a vertical line from the factor to the point axis. The total points, obtained by summing points from all predictors, correspond to the risk of malignant tumors when a vertical line is drawn to the risk axis. The nomogram's cutoff was determined by calculating the total points for all patients based on its application to the training set. Subsequently, we evaluated the predictive performance of the total points using ROC analysis, with the cutoff of the total points in ROC analysis serving as the nomogram's cutoff. This cutoff point was selected to maximize the Youden Index, a metric calculated as "Sensitivity + Specificity—1," ensuring an optimal balance between sensitivity

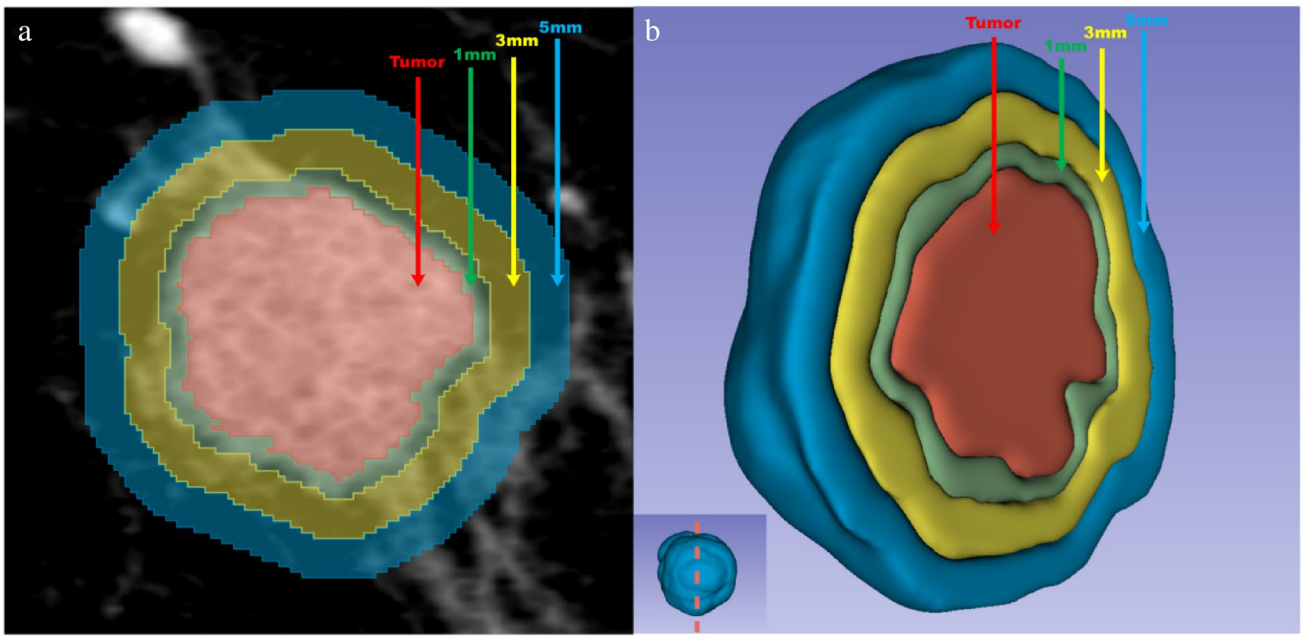

Fig. 3 Visualization of tumors region of interest (ROI) and peritumoral areas. **a** Coronal view displaying the tumors ROI and peritumoral areas. **b** 3D cross-sectional view presenting a detailed representation of the tumors ROI and peritumoral areas. The tumor ROI is highlighted in red (red arrow), indicating its location within the breast tissue. The green mask represents the peritumoral area situated 1mm away from the tumors margin, visible in both the coronal view and 3D display (green arrow). The yellow mask represents the peritumoral area between 1 and 3 mm from the tumors margin (yellow arrow), while the blue mask represents the peritumoral area between 3 and 5 mm away from the tumors margin (blue arrow)

and specificity [22]. The predictive accuracy of this cutoff was further validated in the test set through the utilization of a confusion matrix. We evaluated the nomogram's effectiveness using AUCs, accuracy, sensitivity, and specificity in both the training and test sets. Calibration curves in both sets gauged agreement between observed outcomes and nomogram predictions. Decision Curve Analysis (DCA) assessed the nomogram's added value.

Statistical analysis

ICC interpretation: 0.00–0.20 (poor), 0.21–0.40 (fair), 0.41–0.60 (moderate), 0.61–0.80 (good), 0.81–1.00 (excellent) [23]. Detected associations were deemed significant for p-values < 0.05 in the Spearman correlation test. The differences in quantitative features were compared using either the independent t-test or Mann–Whitney U test, depending on the data distribution. The data were presented as either the mean with standard deviation (SD) or the median with interquartile range (IQR), depending on the distribution of the data. A significance level of p-values < 0.05 was considered statistically significant. AUC values for two peritumoral ΔHU values were compared using the Delong test. Logistic regression yielded Odds ratio (OR) and 95% confidence interval (CI). Features meeting criteria (Adjusted OR > 1, p-values < 0.05) in multivariate logistic regression were considered independent predictors. Statistical analysis used SPSS (v27.0), R (v4.2.2; https://www.r-project.org), and Python (v3.11.3; https://www.python.org).

Result

Patients

Our study included 234 lesions from female patients with an average age of 50.2 (SD ± 9.2) years. The training set comprised 164 patients, including 89 with benign tumors and 75 with malignant breast tumors. The test set consisted of 70 patients, with 29 diagnosed with benign tumors and 41 with malignant breast tumors. A detailed summary of patient characteristics and histopathological results is given in Table 1.

Measurement of quantitative features and comparison of peritumoral ΔHU values

All quantitative features and ROI measurements exhibited good to excellent (0.75–0.97) agreement in the ICC (Supplemental Fig. 1). The Spearman correlation test indicated no statistically significant correlations between features and measurements with necrosis or with peritumoral DCIS in all the malignant patients (Supplemental Tables 1 and 2). Table 2 provides a comprehensive summary of quantitative features and ROI measurements.

Although peritumoral ΔHU 1(AUC = 0.753, 95%CI = 0.679 − 0.826) exhibited a slightly higher AUC than peritumoral ΔHU 2(AUC = 0.738, 95%CI = 0.662 − 0.814), the difference was not statistically significant (Delong test, $p = 0.391$). Based on its marginally better performance, peritumoral ΔHU 1 was selected as the preferred feature to complement the quantitative features for features selection. The ROCs of peritumoral ΔHU values are shown in Fig. 4.

Quantitative features selection

Significant differences were observed in surface area, volume, CE HU, ΔHU, and peritumoral ΔHU 1 between benign and malignant breast tumors in the training set (Table 2). The results of the univariate logistic regression analysis indicated that surface area, volume, CE HU, ΔHU, and peritumoral ΔHU 1 met the criteria of having a Crude OR greater than 1 and a p-value less than 0.05 in the training set. However, in the multivariate logistic regression analysis, only the surface area, ΔHU, and peritumoral ΔHU 1 met the criteria of having an Adjusted OR greater than 1 and a p-value less than 0.05 in the training set, as shown in Table 3. They were identified as independent predictors of malignant breast tumors**.**

Development and validation of the nomogram model

The nomogram was constructed using the independent predictors of malignant breast tumors. In the ROC analysis of total points from the nomogram in the training set, the established cutoff for predicting benign and malignant tumors is 21.583 points (specificity: 0.809, sensitivity: 0.960) (Fig. 5a). Validation in the test set using the confusion matrix (Fig. 5b) yielded an accuracy of 0.829, precision of 0.978, recall of 0.732, and an F1-Score of 0.833. Figure 6 illustrates the nomogram with the applied cut-off, which demonstrated an AUC of 0.940 (95% CI 0.900–0.940) in the training set and 0.970(95% CI 0.940–0.970) in the test set, indicating excellent predictive performance. The accuracy of the nomogram was 0.878 in the training set and 0.928 in the test set. The specificity was 0.809 in the training set and 0.897 in the test set, while the sensitivity was 0.960 in the training set and 0.951 in the test set (Table 4).

Calibration of the nomogram revealed a favorable correspondence between risk estimation and pathological confirmation, providing confidence in its reliability and accuracy (Fig. 7a–b). The DCA curves in both sets indicated that utilizing the nomogram for predicting malignant probability adds more benefit than adopting either a diagnose-none or

Table 1 Summary of patient characteristics and distribution of histopathological results

Characteristics	Training set		*P* value	Test set		*P* value	$p^{\#}$ value	All		*P* value
	Benign ($n=89$)	Malignant ($n=75$)		Benign ($n=29$)	Malignant ($n=41$)			Benign ($n=118$)	Malignant ($n=116$)	
Age	47.00 (45.00,55.00)	51.00 (43.50,60.00)	0.184	46.00 (44.00,49.00)	51.00 (47.00,58.00)	0.001	0.667	47.00 (45.00,52.00)	51.00 (44.00,58.00)	0.007
Lesion location (%)			0.274			0.204	0.450			0.191
LIQ	26(29.2)	23(30.7)		9(31.0)	6(14.6)			35(29.7)	29(25.0)	
LOQ	22(24.7)	18(24.0)		6(20.7)	17(41.5)			28(23.7)	35(30.2)	
UIQ	16(18.0)	21(28.0)		6(20.7)	9(22.0)			22(18.6)	30(25.9)	
UOQ	25(28.1)	13(17.3)		8(27.6)	9(22.0)			33(28.0)	22(19.0)	
Lesion detection (%)			0.947			0.843	0.328			0.782
Palpable mass	42(47.2)	35(46.7)		12(41.4)	16(39.0)			54(45.8)	51(44.0)	
Screening reveals	47(52.8)	40(53.3)		17(58.6)	25(61.0)			64(54.2)	65(56.0)	
Menstrual status(%)			0.278			0.036	0.172			0.070
Menopausal	25(28.1)	27(36.0)		3(10.3)	13(31.7)			28(23.7)	40(34.5)	
Pre-menopausal	64(71.9)	48(64.0)		26(89.7)	28(68.3)			90(76.3)	76(65.5)	
Histopathological results(%)			< 0.001			< 0.001	0.229			< 0.001
Fibroadenoma	79(88.8)	0(0.0)		27(93.1)	0(0.0)			106(89.8)	0(0.0)	
Infiltrating duct carcinoma	0(0.0)	66(88.0)		0(0.0)	38(92.7)			0(0.0)	104(89.7)	
Phyllodes tumor, benign	10(11.2)	0(0.0)		2(6.9)	0(0.0)			12(10.2)	0(0.0)	
Phyllodes tumor, malignant	0(0.0)	9(12.0)		0(0.0)	3(7.3)			0(0.0)	12(10.3)	
Microcalcifications(%)			0.506			0.447	0.350			0.820
With	22(24.7)	22(29.3)		11(37.9)	12(29.3)			33(28.0)	34(29.3)	
Without	67(75.3)	53(70.7)		18(62.1)	29(70.7)			85(72.0)	82(70.7)	
Necrosis(%)			< 0.001			0.019	0.545			< 0.001
With	0(0.0)	21(28.0)		0(0.0)	7(17.1)			0(0.0)	28(24.1)	
Without	89(100.0)	54(72.0)		29(100.0)	34(82.9)			118(100.0)	88(75.9)	
DCIS(%)			< 0.001			0.011	0.488			< 0.001
With	0(0.0)	14(18.7)		0(0.0)	8(19.5)			0(0.0)	22(19.0)	
Without	89(100.0)	61(81.3)		29(100.0)	33(80.5)			118(100.0)	94(81.0)	

LIQ lower inner quadrant, *LOQ* lower outer quadrant, *UIQ* upper inner quadrant, *UOQ* upper outer quadrant

p value indicates the significance of differences between benign and malignant breast tumors

$p^{\#}$ value indicates the significance of differences between the features in training set and test set

Table 2 Summary of quantitative features and ROI measurements

Features and measurements	Training set		*p* value	Test set		*p* value	*p** value	All		*p* value
	Benign ($n=89$)	Malignant ($n=75$)		Benign ($n=29$)	Malignant ($n=41$)			Benign ($n=118$)	Malignant ($n=116$)	
Surface area	1.55 (0.72,4.84)	13.07 (8.81,24.54)	< 0.001	1.84 (1.23,4.96)	11.57 (7.27,17.75)	< 0.001	0.428	1.79 (0.73,4.93)	12.81 (8.24,22.57)	< 0.001
Volume	0.13 (0.04,0.92)	2.49 (1.30,5.66)	< 0.001	0.18 (0.10,0.65)	1.96 (1.20,4.23)	< 0.001	0.49	0.15 (0.04,0.85)	2.40 (1.23,5.16)	< 0.001
NCE HU	39.55 (± 50.58)	42.72 (± 46.98)	0.68	38.41 (± 52.81)	42.42 (± 48.00)	0.742	0.783	39.271 (± 50.69)	42.614 (± 46.93)	0.640
CE HU	98.97 (67.79,126.23)	120.00 (82.17,154.56)	0.009	83.46 (± 61.34)	112.02 (± 54.54)	0.044	0.467	92.62 (± 52.72)	115.96 (± 54.82)	0.001
ΔHU	43.51 (18.41,91.56)	73.61 (59.48,90.26)	< 0.001	43.67 (14.03,63.58)	61.98 (49.91,82.76)	0.002	0.181	43.58 (16.64,76.63)	70.60 (57.78,88.87)	< 0.001
Peritumoral ΔHU1	39.40 (± 19.40)	57.54 (± 18.70)	< 0.001	35.93 (± 16.51)	56.85 (± 16.90)	< 0.001	0.868	38.55 (± 18.72)	57.30 (± 18.01)	< 0.001
Peritumoral ΔHU2	52.27 (± 28.07)	76.37 (± 26.53)	< 0.001	49.02 (± 25.84)	76.25 (± 23.76)	< 0.001	0.688	49.74 (30.36,71.31)	75.89 (58.63,91.70)	< 0.001
$HU_{margin-1\ mm}$	14.04 (± 66.77)	21.20 (± 50.47)	0.447	7.54 (± 72.46)	12.65 (± 50.37)	0.729	0.428	12.44 (± 67.96)	18.17 (± 50.38)	0.465
$HU_{1mm-3\ mm}$	− 25.36 (± 69.37)	− 36.35 (± 44.54)	0.239	− 28.39 (76.19)	− 44.21 (± 49.96)	0.298	0.399	− 26.10 (± 70.78)	− 39.13 (± 46.46)	0.098
$HU_{3mm-5\ mm}$	− 38.23 (± 72.87)	− 55.17 (± 42.88)	0.078	− 41.48 (± 80.87)	− 63.61 (± 48.32)	0.157	0.342	− 39.03 (± 74.57)	− 58.15 (± 44.85)	0.019

NCE HU the whole tumor's CT value without contrast enhanced, *CE HU* the whole tumor's CT value with contrast enhanced, *ΔHU* the degree of the whole tumor's enhancement

p value indicates the significance of differences between benign and malignant breast tumors

*p** value indicates the significance of differences between the features in training set and test set

diagnose-all strategy when the threshold probability falls within the range of 5–94% (Fig. 7c–d).

Discussion

Accurately distinguishing between benign and malignant breast tumors is crucial for informed treatment decisions. Our study identified several quantitative radiologic features of CE CB-BCT as independent predictors for malignant breast tumors, including surface area, ΔHU, and peritumoral ΔHU 1. Building on these findings, we developed and validated a nomogram, providing a non-invasive tool for diagnosing breast tumors. The proposed model exhibited strong performance with an AUC of 0.940 (95% CI 0.900–0.940) in the training set and an AUC of 0.970 (95% CI 0.940–0.970) in the test set. This marks the first study to create a nomogram model based on quantitative features of CE CB-BCT, establishing a cut-off for distinguishing between benign and malignant breast tumors. This novel approach significantly enhances diagnostic precision, with the nomogram's cutoff acting as a crucial threshold in predicting the nature of tumors. Surpassing this cutoff in total points for an individual indicates a higher likelihood of malignant tumors.

Traditional breast tumors evaluation in radiology heavily relies on qualitative assessments, where various tumors characteristics like spiculated, rounded, necrosis, microcalcification, density, type of enhancement, and anatomic relationship to surrounding tissues are subjectively evaluated. Nevertheless, these evaluations may vary based on the radiologists' experience in interpretation [24–26].

In recent years, personalized medicine has gained momentum in the medical field, aiming to provide tailored treatments based on individual patient characteristics and needs, using biomarkers to guide decisions [27]. Imaging has become a valuable technology, offering noninvasive means to obtain biological information about breast tumors. In vivo 2D and 3D measurements of anatomic structures serve as essential quantitative biomarkers, providing measurable, quantifiable, and reproducible parameters crucial for research and clinical decision-making [28, 29]. Several studies have utilized quantitative features of breast imaging to predict malignancy. For instance, Hsu et al. integrated morphological, texture, and Nakagami images, achieving weak sensitivity (< 74.0%) in identifying malignant tumors [30]. Thakur et al. demonstrated the utility of quantitative in vivo MRS assessment of lipid metabolism for identifying malignancies [31]. Mami et al. observed significant differences in IVIM and non-Gaussian diffusion parameters between malignant and benign breast tumors, providing BI-RADS-equivalent scores without contrast agents [32]. Additionally, another study highlighted the superior diagnostic accuracy of quantitative transport mapping velocity and

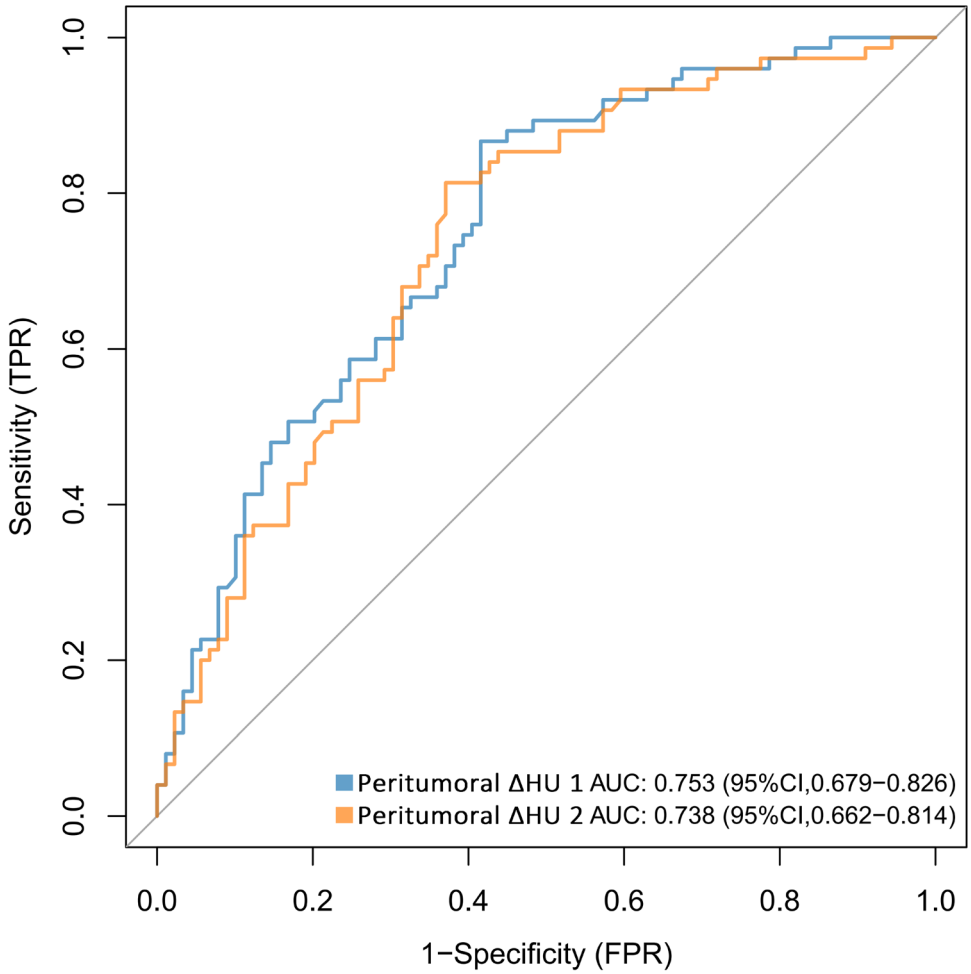

Fig. 4 ROCs of peritumoral ΔHU 1 and peritumoral ΔHU 2. Peritumoral ΔHU 1 exhibited a slightly higher AUC than peritumoral ΔHU 2 without statistically significant ($p = 0.391$, Delong test)

Table 3 Univariate and multivariate logistic regression of quantitative features

Features	Crude OR (95%CI)	Uni-*p* value	Adj OR (95%CI)	Multi-*p* value
Surface area	1.216(1.142,1.309)	< 0.001	3.385(2.155,5.319)	< 0.001
Volume	1.352(1.177,1.605)	< 0.001	0.064(0.022,0.185)	< 0.001
NCE HU	1.001(0.995,1.008)	0.678		
CE HU	1.008(1.002,1.015)	0.008	0.998(0.984,1.011)	0.720
ΔHU	1.015(1.006,1.024)	0.001	1.026(1.004,1.048)	0.018
Peritumoral ΔHU1	1.051(1.032,1.074)	< 0.001	1.068(1.024,1.114)	0.002

NCE HU the whole tumor's CT value without contrast enhanced, *CE HU* the whole tumor's CT value with contrast enhanced, *ΔHU* the degree of the whole tumor's enhancement, *Crude OR* crude odds ratio, *Adj OR* adjusted odds ratio, *CI* confidence interval

volume transfer constant over traditional kinetics methods in differentiating benign from malignant breast tumors [33].

Our study utilizes quantitative features to extract objective information; by incorporating these quantitative features into breast tumors evaluation, we move toward a more personalized approach, delivering precise treatment to patients when needed. This evolution aligns with personalized medicine's goals and has the potential to enhance diagnostic accuracy and treatment outcomes in breast tumors management.

In our study, we investigated various features for breast tumors classification, and among them, surface area, ΔHU, and peritumoral ΔHU 1 emerged as independent predictors of malignant breast tumors. The surface area of a tumors, defined as the total outer boundary area, serves as an indicator for evaluating tumors size, which is a critical prognostic factor in breast tumors [28, 29]. Traditional measurement methods using linear measurements in two dimensions can be challenging when tumors grow diffusely, making accurate

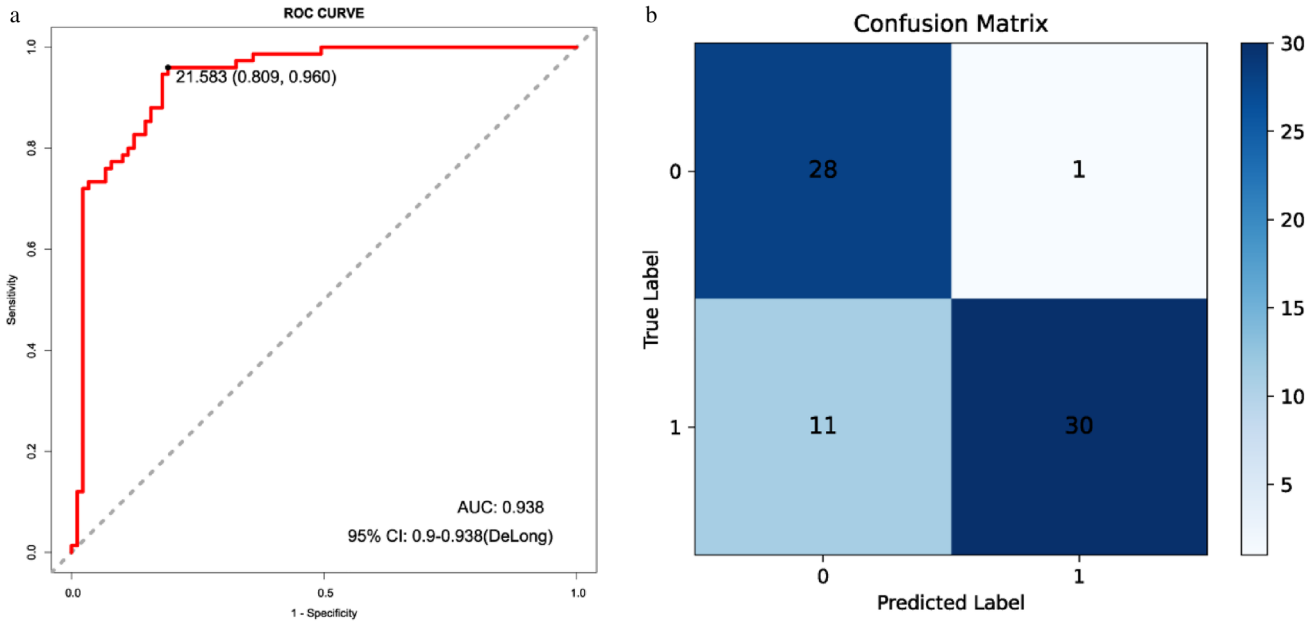

Fig. 5 **a** ROC curves of total points from nomogram in training set with optimal cutoff-based Youden index. **b** Confusion matrix illustrating true label vs. predicted label for predicting benign and malignant tumors, as evaluated on the test set

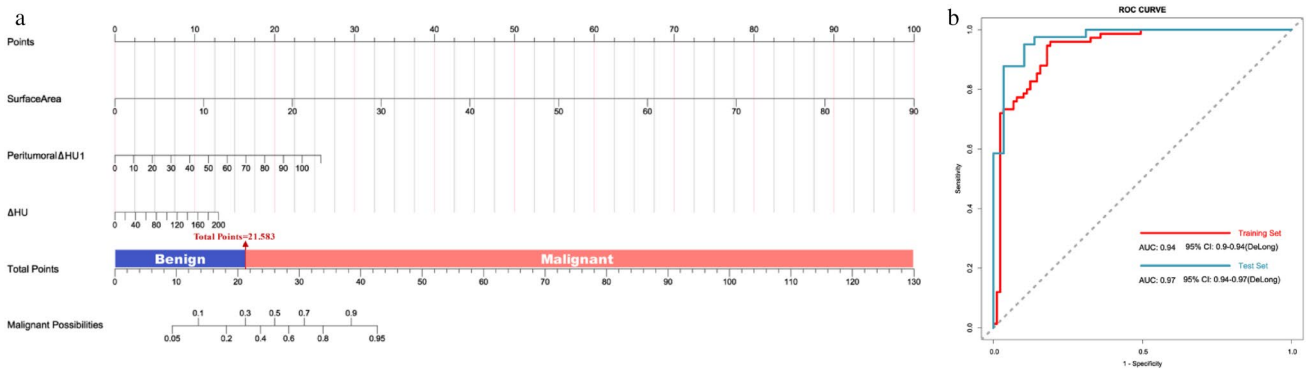

Fig. 6 **a** Nomogram for predicting malignant breast tumors, including the applied cutoff. The cutoff for malignant breast tumors was 21.583 points calculated by the nomogram (red mark). **b** Performance of the nomogram in the training and test set is expressed as area under the ROC curve (AUC)

Table 4 Diagnostic performances of the nomogram

Model	Training set					Test set				
	AUC	95CI%	ACC	SPE	SEN	AUC	95CI%	ACC	SPE	SEN
Nomogram	0.940	0.900–0.940	0.878	0.809	0.960	0.970	0.940–0.970	0.928	0.897	0.951

AUC Area under curve, *CI* confidence intervals, *ACC* accuracy, *SEN* sensitivity, *SPE* specificity

size assessment difficult [30]. To overcome this limitation, we employed three-dimensional spatial analysis, providing a more accurate measurement of tumors size. Malignant tumors, characterized by uncontrolled and disorganized growth, tend to have greater surface unevenness, resulting in larger surface areas, and benign tumors exhibit smoother surface variations, leading to lower surface area measurements [34–36].

We defined and selected peritumoral ΔHU values as a measurement indicator for the peritumoral region and explored its potential as a prediction factor of breast tumors malignancy. The peritumoral region, surrounding the

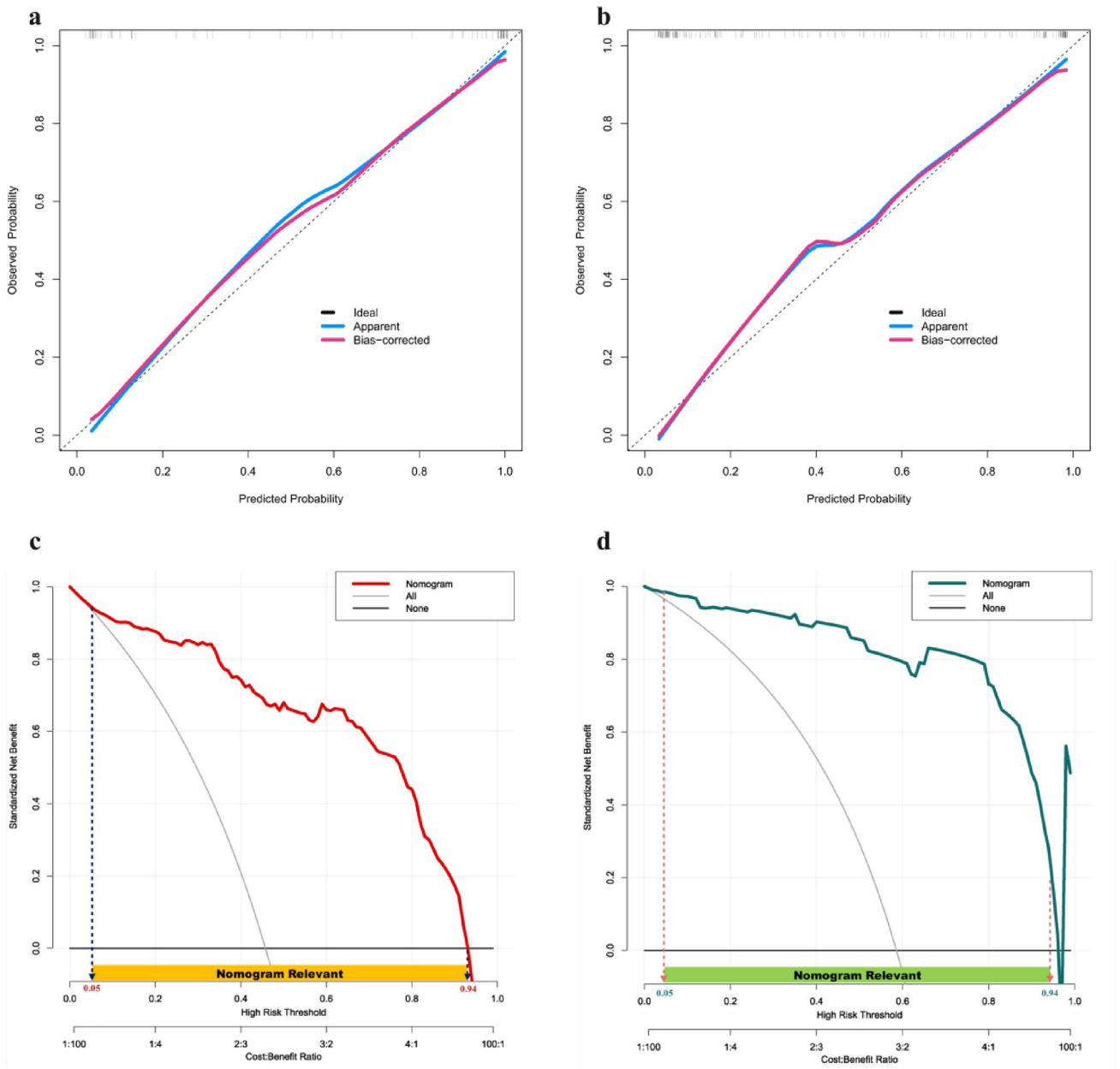

Fig. 7 Calibration curves for the nomogram in training set **a** and test set **b** assess agreement between predicted malignant probabilities and actual outcomes. Each plot includes a rug chart showing the distribution of predicted risks. The 45-degree dotted line represents ideal prediction, while the solid line depicts the nomogram's performance. A closer fit to the diagonal dotted line indicates better prediction. The blue line shows the apparent calibration curve, illustrating the relationship between predicted and observed probabilities. The pink line represents the bias-corrected calibration curve, addressing overfitting or optimistic bias for a more realistic estimate on new data. The DCA curve of the nomogram in training set **c** and test set **d**. The red and green line represents the nomogram. The gray line represents the assumption that all patients are diagnosed as malignant. The black line represents the assumption that none of the patients are diagnosed as malignant. The DCA curves reveals that if the threshold probability is set between 5 and 94%, using the proposed nomogram to detect malignant breast tumors is more advantageous than either the treat-all regimen or the treat-none regimen

tumors, has been found to provide valuable information for diagnosing and predicting prognosis due to tumors invasion, tissue reactions, and changes [37–42]. The density of the peripheral tissue may reflect the stromal and inflammatory response to the tumors, which may vary depending on the type and aggressiveness of the cancer. By calculating peritumoral ΔHU values based on an enhancement method, we aimed to quantitatively assess the perfusion of the peritumoral area. Malignant tumors tend to invade the surrounding tissue, resulting in increased perfusion in the peritumoral

region due to tumors infiltration [40]. Previous studies have emphasized that peritumoral perfusion can differentiate different risk levels of breast tumors and predict biomarkers associated with the aggressiveness of breast malignancies [43, 44]. Additionally, dividing the peritumoral tissue into circles at various distances from the tumors margin has been explored in previous studies, allowing for an examination of tissue changes from the proximity of the tumors to the distant field [45–48]. Our results also support the consideration of proximal peritumoral tissue by defining two peritumoral ΔHU values and comparing their performance in predicting malignant tumors.

Our study also revealed that the ΔHU, reflecting the internal enhancement of the breast tumors, emerged as a significant independent predictor of breast tumors malignancy. Tumors cells require neovascularization for their survival, growth, invasion, and spread. The enhancement of a breast tumors on imaging is not only associated with micro vessel density, neovascularization, and prognostic parameters but also related to factors such as vasculature leakage (capillary permeability), contrast agent delivery (perfusion or diffusion), and the volume of extravascular space [49–51]. The enhancement patterns observed in breast imaging can be utilized to differentiate between benign and malignant breast tumors [52–55]. However, the conventional approach to obtaining enhancement patterns is variable and less reproducible due to different measurement methods from subjective differences among radiologists, leading to variations in visual perception. In the case of CB-BCT, some studies have defined ΔHU based on the maximum section of a suspicious lesion in a coronal view with a slice thickness of 2.7 mm [10, 56]. In our study, we measured the ΔHU of the entire tumors, offering a quantitative method to assess breast enhancement and avoid variations caused by observer-related factors.

Traditional radiology methods for breast tumors diagnosis, combined with biopsies for confirmation, also have limitations in their approach. Mammography, with a sensitivity ranging from 67.3 to 93.3%, often yields negative biopsy results for suspicious lesions [57, 58]; challenges with mammography include the potential for mistaking fibro glandular tissue as lesions [59]. Breast MRI, while limited by cost, availability, and contraindications, also exhibits slightly lower specificity and lead to unnecessary procedures [60, 61]. CB-BCT, a 3D imaging method, exhibits superior sensitivity, patient comfort, shorter examination time, fewer contraindications, and better specificity compared to mammography, the increased specificity may be attributed to effective contrast agent application [8, 13, 60–63]. Moreover, CE CB-BCT shows promise as an alternative imaging modality for the individuals with contraindications to MRI such as the presence of ferromagnetic implants, concerns about gadolinium deposition, or in regions with limited MRI availability [64]. Additionally, the quantitative features of CE CB-BCT in our study provide a more objective and accurate assessment of breast tumors malignancy.

There were some limitations in this study. First, being a single-center study focusing solely on Chinese females limits the generalizability of the conclusions. Second, NME lesions may impact conclusions, warranting further investigation of applicable quantitative radiologic features for NME. While NME diagnosis poses challenges due to mixed tumors tissues and stroma, certain enhancement features like maximum CT value and ΔHU remain valuable. Third, a limitation of CE CB-BCT is its inappropriateness for disease screening in women who are planning to conceive. However, this is not limited to the demographic of adult or elderly women who are more prone to developing breast cancer, because CE CB-BCT alone has demonstrated comparable diagnostic accuracy with reduced radiation exposure [65]. Therefore, in future work, we may perform CE CB-BCT alone to reduce radiation exposure without compromising diagnostic accuracy. Finally, the sample size taken in this study was limited, and the conclusions drawn need further validation.

Conclusion

In conclusion, our study identifies quantitative radiologic features of CE CB-BCT that effectively predict benign and malignant breast tumors. By integrating these features into a nomogram-based diagnostic system, we present a more accurate and objective approach for diagnosing breast tumor. This system enhances classification precision, addressing the diagnostic ambiguity frequently encountered in clinical practice. The implementation of these findings has the potential to improve the reliability and effectiveness of breast tumor management.

Supplementary Information The online version contains supplementary material available at https://doi.org/10.1007/s11547-024-01803-0.

Acknowledgements The authors thank the patients for their willingness to cooperate with our study. The authors of this manuscript declare no relationships with any companies, whose products or services may be related to the subject matter of the article. This work was supported by the National Key R&D Program of China (2020YFA0714002). The funders had no role in study design, data analysis, decision to publish, or preparation of the manuscript.

Author contributions TS contributed to the conception and design of the study, completed image acquisition and analysis, interpreted the data, drafted the manuscript, and provided substantial manuscript revisions. YZ contributed to the study's conception and design, data interpretation, and manuscript revision. HY contributed to the image acquisition and analysis. ZO contributed to the completed image acquisition and analysis, the conception and design of the study. JF and LL contributed to the image acquisition. FL contributed to the study's conception and design, and manuscript revision.

Funding This work was supported by the National Key R&D Program of China (2020YFA0714002) and Joint project of Chongqing Health Commission and Science and Technology Bureau (No. 2022ZDXM006 and 2022QNXM015) and Key Project of Technological Innovation and Application Development of Chongqing Science and Technology Bureau (No. CSTC2021jscxksbN0030).

Declarations

Conflict of interest The authors declare that they have no competing interests.

Ethical approval Institutional Review Board approval was obtained (2022-K313).

Consent to participation This retrospective study was approved by the institutional review board of our hospital (2022-K313). The requirement for the patients' informed consent was waived.

Consent for publication In this manuscript, all images analyzed are entirely unidentifiable, and the only individual detail provided is the age of the participants.

References

1. Arnold M, Morgan E, Rumgay H et al (2022) Current and future burden of breast cancer: global statistics for 2020 and 2040. Breast 66:15–23
2. Wu J, Li C, Gensheimer M et al (2021) Radiological tumor classification across imaging modality and histology. Nat Mach Intell 3:787–798
3. Spak DA, Plaxco JS, Santiago L, Dryden MJ, Dogan BE (2017) BI-RADS fifth edition: a summary of changes. Diagn Interv Imaging 98:179–190
4. Ku YJ, Kim HH, Cha JH et al (2016) Correlation between MRI and the level of tumor-infiltrating lymphocytes in patients with triple-negative breast cancer. AJR Am J Roentgenol 207:1146–1151
5. Moon HG, Kim N, Jeong S et al (2015) The clinical significance and molecular features of the spatial tumor shapes in breast cancers. PLoS ONE 10:e0143811
6. He N, Wu Y-P, Kong Y et al (2016) The utility of breast cone-beam computed tomography, ultrasound, and digital mammography for detecting malignant breast tumors: a prospective study with 212 patients. Eur J Radiol 85:392–403
7. Zhao B, Zhang X, Cai W, Conover D, Ning R (2015) Cone beam breast CT with multiplanar and three dimensional visualization in differentiating breast masses compared with mammography. Eur J Radiol 84:48–53
8. Wienbeck S, Fischer U, Luftner-Nagel S, Lotz J, Uhlig J (2018) Contrast-enhanced cone-beam breast-CT (CBBCT): clinical performance compared to mammography and MRI. Eur Radiol 28:3731–3741
9. Uhlig J, Uhlig A, Biggemann L, Fischer U, Lotz J, Wienbeck S (2019) Diagnostic accuracy of cone-beam breast computed tomography: a systematic review and diagnostic meta-analysis. Eur Radiol 29:1194–1202
10. Ma Y, Liu A, O'Connell AM et al (2021) Contrast-enhanced cone beam breast CT features of breast cancers: correlation with immunohistochemical receptors and molecular subtypes. Eur Radiol 31:2580–2589
11. Zhu Y, Zhang Y, Ma Y et al (2020) Cone-beam breast CT features associated with HER2/neu overexpression in patients with primary breast cancer. Eur Radiol 30:2731–2739
12. Li H, Yin L, He N et al (2019) Comparison of comfort between cone beam breast computed tomography and digital mammography. Eur J Radiol 120:108674
13. Wienbeck S, Lotz J, Fischer U (2017) Review of clinical studies and first clinical experiences with a commercially available cone-beam breast CT in Europe. Clin Imaging 42:50–59
14. Goto T, Camargo CA, Faridi MK, Freishtat RJ, Hasegawa K (2019) Machine learning-based prediction of clinical outcomes for children during emergency department triage. JAMA Netw Open 2:e186937
15. Collins GS, Reitsma JB, Altman DG, Moons KGM (2015) Transparent reporting of a multivariable prediction model for individual prognosis or diagnosis (TRIPOD): the TRIPOD statement. Ann Intern Med 162:55–63
16. Steyerberg EW, Bleeker SE, Moll HA, Grobbee DE, Moons KGM (2003) Internal and external validation of predictive models: a simulation study of bias and precision in small samples. J Clin Epidemiol 56:441–447
17. Steyerberg E (2009) Clinical prediction models: a practical approach to development, validation, and updating
18. American College of Radiology (ACR) Committee on Drugs and Contrast Media (2021) ACR manual on contrast media. Version 2021. Available via https://www.acr.org/-/media/ACR/Files/Clinical-Resources/Contrast_Media.pdf
19. European Society of Urogenital Radiology (ESUR) Contrast Medium Safety Committee (2019) ESUR guidelines on contrast agents. version 10.0. Available via https://www.esur.org/wp-content/uploads/2022/03/ESUR-Guidelines-10_0-Final-Version.pdf
20. Fedorov A, Beichel R, Kalpathy-Cramer J et al (2012) 3D slicer as an image computing platform for the quantitative Imaging network. Magn Reson Imaging 30:1323–1341
21. Shrout PE, Fleiss JL (1979) Intraclass correlations: uses in assessing rater reliability. Psychol Bull 86:420–428
22. Vigneshwar NG, Moore EE, Moore HB et al (2022) Precision medicine: clinical tolerance to hyperfibrinolysis differs by shock and injury severity. Ann Surg 275:e605–e607
23. Yu Q, Ning Y, Wang A et al (2023) Deep learning-assisted diagnosis of benign and malignant parotid tumors based on contrast-enhanced CT: a multicenter study. Eur Radiol 33:6054–6065
24. Tagliafico AS, Piana M, Schenone D, Lai R, Massone AM, Houssami N (2020) Overview of radiomics in breast cancer diagnosis and prognostication. Breast 49:74–80
25. Michaels AY, Chung CSW, Frost EP, Birdwell RL, Giess CS (2017) Interobserver variability in upgraded and non-upgraded BI-RADS 3 lesions. Clin Radiol 72:694.e691-694.e696
26. Eghtedari M, Chong A, Rakow-Penner R, Ojeda-Fournier H (2021) Current status and future of BI-RADS in multimodality imaging, from the AJR special series on radiology reporting and data systems. AJR Am J Roentgenol 216:860–873
27. European Society of R (2015) Medical imaging in personalised medicine: a white paper of the research committee of the European society of radiology (ESR). Insights Imaging 6:141–155
28. O'Connor JPB, Aboagye EO, Adams JE et al (2017) Imaging biomarker roadmap for cancer studies. Nat Rev Clin Oncol 14:169–186
29. Galati F, Moffa G, Pediconi F (2022) Breast imaging: beyond the detection. Eur J Radiol 146:110051
30. Hsu SM, Kuo WH, Kuo FC, Liao YY (2019) Breast tumor classification using different features of quantitative ultrasound parametric images. Int J Comput Assist Radiol Surg 14:623–633
31. Thakur SB, Horvat JV, Hancu I et al (2019) Quantitative in vivo proton MR spectroscopic assessment of lipid metabolism: value for breast cancer diagnosis and prognosis. J Magn Reson Imaging JMRI 50:239–249
32. Iima M, Kataoka M, Kanao S et al (2018) Intravoxel incoherent motion and quantitative non-Gaussian diffusion MR imaging:

evaluation of the diagnostic and prognostic value of several markers of malignant and benign breast lesions. Radiology 287:432–441
33. Zhang Q, Spincemaille P, Drotman M et al (2022) Quantitative transport mapping (QTM) for differentiating benign and malignant breast lesion: Comparison with traditional kinetics modeling and semi-quantitative enhancement curve characteristics. Magn Reson Imaging 86:86–93
34. Liney GP, Sreenivas M, Gibbs P, Garcia-Alvarez R, Turnbull LW (2006) Breast lesion analysis of shape technique: semiautomated vs. manual morphological description. Journal of Magnetic Resonance Imaging : JMRI 23:493–498
35. Reiser I, Nishikawa RM, Giger ML, Boone JM, Lindfors KK, Yang K (2012) Automated detection of mass lesions in dedicated breast CT: a preliminary study. Med Phys 39:866–873
36. Hanahan D, Weinberg RA (2011) Hallmarks of cancer: the next generation. Cell 144:646–674
37. Mohammed ZM, McMillan DC, Edwards J et al (2013) The relationship between lymphovascular invasion and angiogenesis, hormone receptors, cell proliferation and survival in patients with primary operable invasive ductal breast cancer. BMC Clin Pathol 13:31
38. Heaphy CM, Griffith JK, Bisoffi M (2009) Mammary field cancerization: molecular evidence and clinical importance. Breast Cancer Res Treat 118:229–239
39. Uematsu T (2015) Focal breast edema associated with malignancy on T2-weighted images of breast MRI: peritumoral edema, prepectoral edema, and subcutaneous edema. Breast Cancer (Tokyo, Japan) 22:66–70
40. Lee KM, Kim EJ, Jahng GH, Park BJ (2014) Value of perfusion weighted magnetic resonance imaging in the diagnosis of supratentorial anaplastic astrocytoma. J Korean Neurosurg Soc 56:261–264
41. Schwertfeger KL, Cowman MK, Telmer PG, Turley EA, McCarthy JB (2015) Hyaluronan, inflammation, and breast cancer progression. Front Immunol 6:236
42. Cheon H, Kim HJ, Kim TH et al (2018) Invasive breast cancer: prognostic value of peritumoral edema identified at preoperative MR imaging. Radiology 287:68–75
43. Shin HJ, Park JY, Shin KC et al (2016) Characterization of tumor and adjacent peritumoral stroma in patients with breast cancer using high-resolution diffusion-weighted imaging: correlation with pathologic biomarkers. Eur J Radiol 85:1004–1011
44. Fan M, He T, Zhang P, Zhang J, Li L (2017) Heterogeneity of diffusion-weighted imaging in tumours and the surrounding stroma for prediction of Ki-67 proliferation status in breast cancer. Sci Rep 7:2875
45. Chen JH, Zhang Y, Chan S, Chang RF, Su MY (2018) Quantitative analysis of peri-tumor fat in different molecular subtypes of breast cancer. Magn Reson Imaging 53:34–39
46. Obeid JP, Stoyanova R, Kwon D et al (2017) Multiparametric evaluation of preoperative MRI in early stage breast cancer: prognostic impact of peri-tumoral fat. Clin Transl Oncol Off Publ Fed Spanish Oncol Soc Natl Cancer Inst Mexico 19:211–218
47. Braman NM, Etesami M, Prasanna P et al (2017) Intratumoral and peritumoral radiomics for the pretreatment prediction of pathological complete response to neoadjuvant chemotherapy based on breast DCE-MRI. Breast Cancer Res BCR 19:57
48. Zhou J, Zhang Y, Chang KT et al (2020) Diagnosis of benign and malignant breast lesions on DCE-MRI by using radiomics and deep learning with consideration of peritumor tissue. J Magn Reson Imaging 51:798–809
49. Çetinkaya E, Yıldız Ş, Otçu H, Sharifov R, Çelik Yabul F, Alkan A (2022) The value of adjacent vessel sign in malignant breast tumors. Diagn Interv Radiol 28:463–469
50. Caiazzo C, Di Micco R, Esposito E et al (2018) The role of MRI in predicting Ki-67 in breast cancer: preliminary results from a prospective study. Tumori 104:438–443
51. Shin HJ, Kim HH, Shin KC et al (2016) Prediction of low-risk breast cancer using perfusion parameters and apparent diffusion coefficient. Magn Reson Imaging 34:67–74
52. Mann RM, Kuhl CK, Kinkel K, Boetes C (2008) Breast MRI: guidelines from the European society of breast imaging. Eur Radiol 18:1307–1318
53. Macura KJ, Ouwerkerk R, Jacobs MA, Bluemke DA (2006) Patterns of enhancement on breast MR images: interpretation and imaging pitfalls. Radiographics 26(6):1719–1734
54. Kuhl CK, Mielcareck P, Klaschik S et al (1999) Dynamic breast MR imaging: are signal intensity time course data useful for differential diagnosis of enhancing lesions? Radiology 211:101–110
55. Huang JS, Pan HB, Yang TL et al (2020) Kinetic patterns of benign and malignant breast lesions on contrast enhanced digital mammogram. PLoS ONE 15:e0239271
56. Prionas ND, Lindfors KK, Ray S et al (2010) Contrast-enhanced dedicated breast CT: initial clinical experience. Radiology 256:714–723
57. Phi X-A, Tagliafico A, Houssami N, Greuter MJW, de Bock GH (2018) Digital breast tomosynthesis for breast cancer screening and diagnosis in women with dense breasts - a systematic review and meta-analysis. BMC Cancer 18:380
58. Sprague BL, Arao RF, Miglioretti DL et al (2017) National performance benchmarks for modern diagnostic digital mammography: update from the breast cancer surveillance consortium. Radiology 283:59–69
59. Dullum JR, Lewis EC, Mayer JA (2000) Rates and correlates of discomfort associated with mammography. Radiology 214:547–552
60. Jochelson MS, Dershaw DD, Sung JS et al (2013) Bilateral contrast-enhanced dual-energy digital mammography: feasibility and comparison with conventional digital mammography and MR imaging in women with known breast carcinoma. Radiology 266:743–751
61. Cong W, Intes X, Wang G (2017) Optical tomographic imaging for breast cancer detection. J Biomed Opt 22:1–6
62. O'Connell AM, Kawakyu-O'Connor D (2012) Dedicated cone-beam breast computed tomography and diagnostic mammography: comparison of radiation dose, patient comfort, and qualitative review of imaging findings in BI-RADS 4 and 5 lesions. J Clin Imaging Sci 2:7
63. O'Connell AM, Karellas A, Vedantham S, Kawakyu-O'Connor DT (2018) Newer technologies in breast cancer imaging: dedicated cone-beam breast computed tomography. Semin Ultrasound CT MR 39:106–113
64. Zhu Y, O'Connell AM, Ma Y et al (2021) Dedicated breast CT: state of the art—part II. Clinical application and future outlook. Eur Radiol 32:2286–2300
65. Uhlig J, Fischer U, Biggemann L, Lotz J, Wienbeck S (2019) Pre- and post-contrast versus post-contrast cone-beam breast CT: can we reduce radiation exposure while maintaining diagnostic accuracy? Eur Radiol 29:3141–3148